A Temperature- and Composition-Dependent Study of H_2SO_4 Aerosol Optical Constants Using Fourier Transform and Tunable Diode Laser Infrared Spectroscopy

R. F. Niedziela,† M. L. Norman, C. L. DeForest, and R. E. Miller*

Department of Chemistry, University of North Carolina, Chapel Hill, North Carolina 27599-3290

D. R. Worsnop

Center for Aerosol and Cloud Chemistry, Aerodyne Research, Inc., Billerica, Massachusetts 01821-3976

Received: April 22, 1999; In Final Form: August 6, 1999

Frequency-dependent optical constants have been determined from the Fourier transform infrared spectra of laboratory-generated liquid sulfuric acid/water aerosols over a range of temperatures and compositions that are relevant to the upper troposphere and lower stratosphere of Earth. The compositions of the particles were determined in situ using a tunable diode laser to monitor equilibrium water vapor pressures. The infrared complex refractive indices of sulfuric acid are shown to be strongly dependent on temperature and composition, because of changes in the equilibrium between sulfate and bisulfate ions. Results from this study also have implications in understanding the temperature dependence of intermolecular interactions within ionic solutions. The database presented here is the most extensive yet available for the liquid solutions of sulfuric acid.

Introduction

Liquid sulfuric acid/water aerosols have a significant influence on a range of atmospheric processes, both in the lower stratosphere and in the troposphere. These particles play an important role in the formation of polar stratospheric clouds (PSCs), providing surfaces on which reservoir chlorine is converted into active chlorine species which are known to catalytically destroy ozone.[1] Sulfate aerosols also serve as cloud condensation nuclei, scatter incoming solar radiation, and absorb outgoing terrestrial infrared radiation.[2] Quantifying the role of sulfuric acid aerosols in atmospheric processes requires, among other things, assessments of particle number density and composition. These values are obtained using remote sensing techniques[3,4] which depend on the availability of accurate complex refractive indices under relevant atmospheric conditions.[2]

Previous studies of the frequency-dependent optical constants of sulfuric acid have been carried out on bulk solutions over a limited range of temperatures and compositions.[5−8] Of these, the data sets of Palmer and Williams (PW)[6] are the most widely used in atmospheric studies,[9−11] even though the measurements were all performed at room temperature. The PW results do show that the refractive indices of sulfuric acid depend strongly upon the composition, normally quoted in sulfuric acid weight percent (wt %). More recent infrared studies of supercooled liquids at low temperature, both in our laboratory[12] and in others[13−15] indicate that the infrared optical properties of sulfuric acid are indeed strongly temperature dependent. In a recent letter from our laboratory[16] and in a paper by Tisdale and coworkers,[17] the temperature dependence of the optical constants has been quantified over a limited range of temperatures and compositions. These two studies are quite different in their approach, however, as the latter was carried out on thin films and the former on laboratory-generated aerosols. Despite the very different approaches, the results of the two studies are in rather good agreement, although there are some differences that have yet to be fully understood.

Perhaps the most challenging aspect of these temperature-dependent studies is accurate determination of the liquid composition. In conventional thin film studies there is no direct determination of the film composition, only that obtained from careful characterization of the deposition process[18−20] or analysis of the film using temperature programmed desorption methods.[21,22] In a previous letter,[16] we reported a few sulfuric acid optical constant data sets that were determined with the aid of a new apparatus. This apparatus makes use of in situ diode laser monitoring of the water partial pressure in equilibrium with the supercooled liquid aerosols to determine their composition. In the present article we give more of the experimental details that are needed to make this approach quantitative (within 1 wt %). This is by far the most accurate method yet reported for determining the composition of liquid aerosol samples used in optical constant measurements. We make use of this method to obtain the most extensive database for liquid sulfuric acid/water yet reported.

Experimental Section

The present experiments were carried out in a new laminar flow aerosol cell, shown schematically in Figure 1. The design is based on an earlier cell used in our laboratory[12,23] and consists of several sections of gold-plated, 7.62 cm diameter copper tubing, thermally separated by thin stainless steel spacers. The temperatures of the various sections are actively and independently controlled to within ±1 K, by applying sufficient resistive heating to each zone to balance the cooling supplied by chilled nitrogen gas. The temperatures were measured using an array of platinum resistance thermometer elements (RTDs) positioned at various locations along the cell. These were interfaced to a computer through a custom built temperature control unit. The entire cell assembly was thermally isolated from the atmosphere in an acrylic vacuum chamber.

* To whom correspondence should be addressed.
† Present address: Department of Chemistry, DePaul University, Chicago, IL.

10.1021/jp991323o CCC: $18.00
Published on Web 09/17/1999

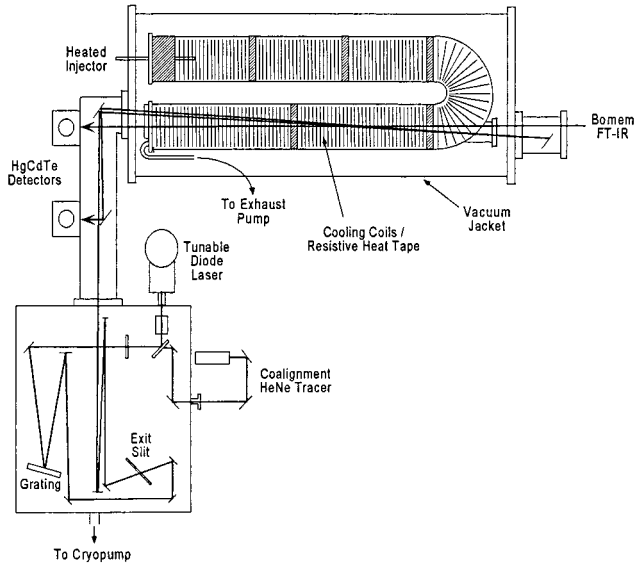

Figure 1. Schematic of aerosol flow cell and tunable diode laser (TDL) apparatus.

Sulfuric acid aerosols were formed outside the cell using a technique developed by Lovejoy et al.[24] In brief, a small pool of concentrated sulfuric acid was placed in the elbow of a simple glass V-shaped tube that was heated to vaporize the liquid. The vapor was then swept out of the elbow and into a room temperature cooling arm of the vaporizer with a metered stream of helium gas. The sudden cooling of the vapor caused it to supersaturate, resulting in the nucleation and growth of concentrated sulfuric acid particles. Of particular importance to the present study, the particle size could easily be varied by changing the temperature of the sulfuric acid pool or the helium buffer gas flow rate.

Once formed, the composition of the particles was easily changed by metering a stream of humidified helium buffer gas into a heated glass mixing bulb, resulting in rapid uptake of the water by the aerosols. The "conditioned" aerosol stream was then directed through a heated stainless steel injector into the first of the upper sections of the flow cell at flow rates ranging from 1 to 2 standard liters per minute. A pump at the other end (in the lower section) of the flow cell was used to maintain a steady-state cell pressure of 300 Torr. The first three sections of the flow cell were necessary to allow for homogeneous mixing of the acid/water solutions, given that the diffusion rates we estimated for water into cold H_2SO_4 droplets[25,26] are quite slow (on the order of seconds), and to ensure that the particles had time to thermally equilibrate with the surrounding buffer gas at the cell temperature. In the present experiments, all of the sections of the flow tube were set to the same temperature. The infrared spectra of the conditioned sulfuric acid aerosols were recorded over a 116 cm long path through the lower sections of the flow cell using a Bomem DA3.02 FT-IR spectrometer. Spectra were recorded from 825 to 4700 cm^{-1} at a resolution of 2 cm^{-1}. The long wavelength end of this range was limited by the cutoff frequency of the BaF_2 windows used to seal each end of the flow cell's lower portion. All of the spectra used in the following analyses represent the co-addition of 100 scans.

Calibration Experiments. As noted above, the key to determining the composition of the aerosols used in the present study was to monitor equilibrium water vapor pressures using absorption spectroscopy. This approach gives much more accurate results than the empirical method developed by Anthony et al.[27] based on the relative areas under various portions of the aerosol spectra, which at best gave results to within ±7 wt %. In particular, this method is not very reliable when the spectra contain a large scattering component,[12] precisely the type we are interested in here. The present approach employs a high-resolution tunable diode laser (TDL) to measure the absorption spectra of individual rovibrational water vapor transitions. The baseline of the extinction data was fit to a polynomial to account for scattering by the aerosols and slowly varying fluctuations in laser intensity over the frequency range. The resulting transmission was then used in a Beer's law analysis to determine the water vapor pressure. When combined with the temperature of the aerosol stream, the aerosol composition can be accurately determined with the aid of the thermodynamic model of Carslaw et al.[28] The diode laser optical system used in the present experiments, shown in Figure 1, is based on the design developed at Aerodyne Research, Inc. The frequency region accessible with the diode used here is centered near 1700 cm^{-1}, corresponding to the ν_2 bending mode of water. To have the dynamic range of pressures ($1-10^{-4}$ Torr) needed to cover the entire temperature and composition range of interest here, it was necessary to use a number of different water vapor transitions with widely different absorption coefficients. The transitions used in the present analysis are listed in Table 1.

TABLE 1: Water Rovibrational Lines Having Center Frequencies ν_o that Were Monitored Using the Tunable Diode Laser to Cover a Range of Vapor Pressures, p_{H_2O}[a]

p_{H2O} (Torr)	ν_o (cm^{-1})	S at 296 K (cm^{-1}/molec·cm^2)	γ_{air} at 296 K (cm^{-1}/atm)	γ_{He} at (T, K) (cm^{-1}/atm)
$\geq 10^{-1}$	1649.418	2.404×10^{-22}	0.0570	0.0126 (250)
$10^{-1} - 10^{-2}$	1750.984	2.830×10^{-20}	0.0430	0.0114 (240)
				0.0116 (230)
$10^{-2} - 10^{-4}$	1751.423	8.509×10^{-20}	0.0428	0.0116 (250)
				0.0118 (225)
				0.0121 (220)
				0.0125 (210)
$10^{-3} - 10^{-6}$	1699.934	2.526×10^{-19}	0.1020	0.0142 (220)

[a] The line strengths S and air broadening coefficients γ_{Air} at room temperature were taken from the HITRAN spectroscopic database,[29] while the helium broadening coefficients γ_{He} were determined in this study at the temperatures shown. For more detailed information on the energy levels for these transitions, the reader is referred to the HITRAN database and the references therein.

Single mode scans of the diode laser were carried out over a 1 cm^{-1} range at a repetition rate of 1 kHz. The laser output passed through a monochromator to ensure that only a single mode was used at all times. Signals from the MCT detector were processed by a fast A/D converter and averaged over a period of one minute. The frequency tuning rate of the laser was calibrated by fitting the center frequencies of several water vapor transitions within a single scan. In cases where only one water vapor transition was available, we added N_2O to the cell to increase the number of transitions available for this fit. The entire TDL system was enclosed in a vacuum chamber pumped by a liquid-nitrogen-cooled trap and was coupled to the flow cell via an evacuated path. This evacuated path was necessary to prevent atmospheric water vapor from interfering with the measurements. As shown in Figure 1, the TDL beam passes twice through the cell to increase the path length and thus improve the detection sensitivity.

Many of the water vapor spectroscopic parameters for transitions used in this study were well documented in the literature.[29] However, quantitative analysis of the vapor pressures was complicated by the fact that the measurements were done in the presence of 300 Torr of helium buffer gas. The buffer was of course needed to suspend the particles and (as discussed

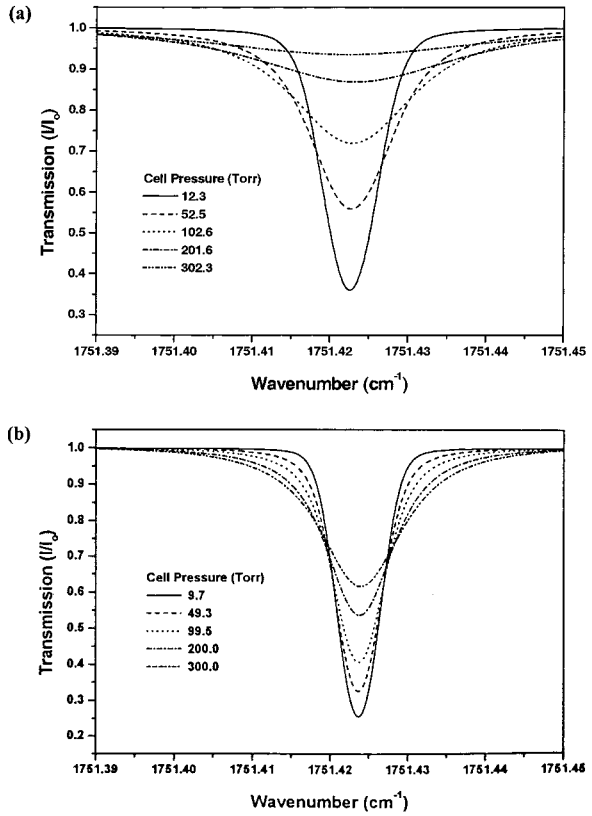

Figure 2. Pressure broadening of the 1751.423 cm^{-1} line of water by (a) nitrogen and (b) helium buffer gases.

below) to ensure that the measured vapor pressures were not influenced by other sections of the cell. Thus the TDL data analysis needed to account for pressure broadening associated with the helium buffer. Figures 2a and 2b show two series of water vapor spectra at 1751.423 cm^{-1}, illustrating the effects of pressure broadening due to nitrogen and helium, respectively. As expected, the pressure broadening in nitrogen is much greater than in helium. Consequently, using helium as a buffer gas provides the particle suspension that is needed, while minimizing the effects of pressure broadening.

For the vapor pressure measurements to be quantitative, it was necessary to determine temperature-dependent pressure broadening coefficients for all of the water lines used in this study. Experimentally, this was accomplished by collecting TDL spectra of the type shown in Figure 2 and fitting the spectral line widths using Voigt profiles,[30] which yielded the pressure broadening coefficients (in cm^{-1}/atm). The results of this study are listed in Table 1, along with the air broadening parameters reported for each transition in the HITRAN database.[29] In comparing these two sets of data, it is clear that the helium broadening coefficients scale proportionally with the air coefficients. In an attempt to account for the weak temperature dependence observed in these data, we calculated the collisionally broadened widths using the expression

$$\alpha_L = \sum_i n_i \sigma_i^2 \left[\frac{2kT}{\pi}\left(\frac{1}{m} + \frac{1}{m_i}\right)\right]^{1/2} \qquad (1)$$

which is derived from elementary kinetic theory.[31] Here, α_L is the Michelson−Lorentz line width (fwhm), n_i is the number density of perturbing molecules (helium), σ_i is the molecular collision diameter, k is Boltzmann's constant, T is the absolute temperature, and m and m_i are the masses of water and helium, respectively. For each transition listed in Table 1, we calculated

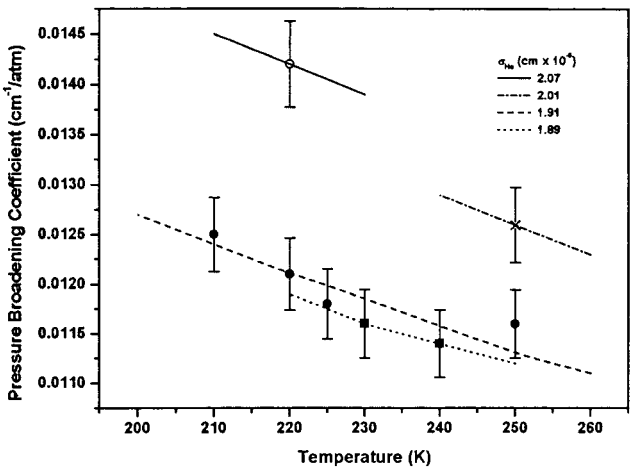

Figure 3. Temperature dependence of the pressure broadening coefficients determined at 1649.934 cm^{-1} (○), 1649.418 cm^{-1} (×), 1751.423 cm^{-1} (●), and 1750.984 cm^{-1} (■) in the present study. The curves resulting from theoretical calculations (discussed in the text) were derived using 2.5×10^{-8} cm for the molecular collision diameter σ for helium and iterating that value to determine the best fit through each data set. Final values for σ_{He} corresponding to each frequency are listed in the legend.

α_L as a function of n_i for each relevant temperature. The results of these calculations are shown in Figure 3, along with the experimental data points. By adjusting σ_i for each transition, we obtained theoretical curves that best fit the data points. This simple model clearly gives a temperature dependence that is in good agreement with the measured values for those transitions where a range of temperatures was used.

To test the accuracy of our approach for determining the water vapor pressures, we carried out a series of vapor pressure measurements in equilibrium with water ice, both as a freely suspended flowing aerosol stream and a coating on the cell wall. In all cases, the cell was pressurized to 300 Torr with helium. The results of these experiments are shown in Figure 4 and are in excellent agreement with the values reported by Marti and Mauersberger for bulk water ice.[32] This clearly shows that the TDL system can provide quantitative measurements of the water vapor pressures in the presence of the helium buffer gas.

The final issue we wish to address is related to the cell temperature that actually controls the measured vapor pressure. At low pressure, where the vapor diffusion time from one part of the cell to another is short, the vapor pressure could be completely determined by a cold spot somewhere in the cell. Given the complexity of the current cell geometry, this could present serious problems. Fortunately, the high helium buffer gas pressure is advantageous here. To illustrate this, we conducted several experiments where the water vapor pressure was measured in an ice-coated cell, as a function of the helium buffer pressure. To emphasize "cross talk" between the various parts of the cell, we held the upper sections of the cell either colder (160 K) or warmer (270 K) than the lower observation region (214 K). The results of this study are shown in Figure 5. At high helium buffer pressures, the measured water vapor pressure is in excellent agreement with that expected[32] at the temperature of the lower section of the cell. However, at low helium buffer pressures, we see a systematic deviation from this value, to either higher or lower vapor pressures, depending upon whether the upper section of the cell is warmer or colder than the observation region, respectively. Clearly in this pressure regime there is diffusion of water vapor from one section of the cell to another, such that the vapor pressures measured in the lower section are affected by the temperature of the upper

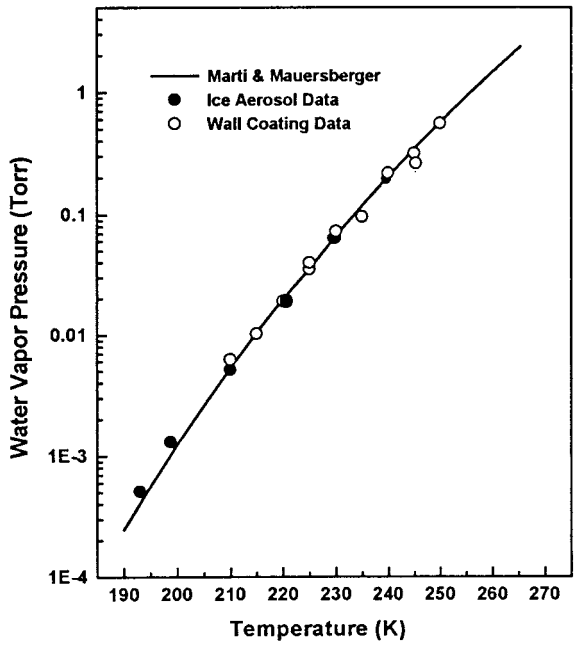

Figure 4. Equilibrium water vapor pressures measured using the tunable diode laser for both ice aerosols (solid circles) and ice coating on the cell walls (open circles). The solid line represents the results of Marti and Mauersberger[32] for bulk water ice. Note that the present data were all collected in 300 Torr of helium buffer gas.

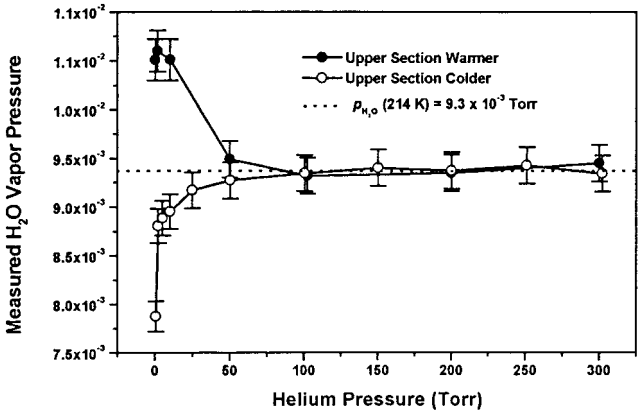

Figure 5. An illustration of the thermal isolation between the various flow cell sections provided by buffer gas pressure. At helium pressures less than 100 Torr, the water vapor pressure over ice measured with the tunable diode laser is either higher or lower than expected, when the upper section is warmer (closed circles) or colder (open circles), respectively, than the lower section. The error bars of ±2% represent the uncertainty resulting primarily from cell temperature measurement.

section. At cell pressures above 100 Torr, however, the vapor diffusion between the various parts of the cell is sufficiently slow so that they are effectively isolated from one another. Thus under the conditions used in the optical constant measurements, the lower section is isolated and the vapor pressures are indicative of the equilibrium with the local aerosol stream.

Optical Constant Calculations. Complex refractive indices were retrieved directly from infrared aerosol extinction spectra using a procedure reported in detail previously.[23,33] Briefly, a nonscattering, small particle spectrum was used to estimate, within a scaling factor, the frequency-dependent, imaginary component of the complex refractive indices. Although this estimate is strictly valid only for bulk materials and not finite-sized particles,[34] it serves as a convenient approximation to initiate the retrieval calculation. The imaginary indices were used in a subtractive Kramers−Kronig transform[34] to calculate the corresponding frequency-dependent real indices. Mie scattering theory was then used in combination with this refractive index data set to simulate a scattering, large particle spectrum, assuming a log-normal distribution of particle sizes. The scattering aerosol spectrum is sensitive to both the real and imaginary components of the refractive index. We have found that for sufficiently strong scatterers, the scaling factor for the imaginary refractive index can be uniquely determined by fitting the Mie calculations to the aerosol spectrum. The parameters iterated in this fit include this scaling factor and the median radius and width that define the particle size distribution. As we have done successfully in our NAD optical constant studies,[33] it was necessary once during each of the present calculations to apply a mathematical correction[34] that accounts for the small amount of scattering actually present in the initial small particle spectrum.

The subtractive Kramers−Kronig transform used in our optical constant retrieval method requires a value for the real refractive index at a single "anchor" point in the spectral range of the calculation where no significant absorption features are present.[35] Unfortunately, the real refractive indices are not available at the anchor point chosen here (3800 cm^{-1}) for all compositions and temperatures. As a result, we had to estimate these values by fitting the room-temperature real refractive index data of Palmer and Williams[6] at 3800 cm^{-1} (for 25, 38, 75, 85, and 96.4 wt % sulfuric acid), along with the real index of liquid water (i.e., 0 wt % sulfuric acid) from Hale and Querry,[36] to a quadratic function. This function was then used to interpolate the room-temperature data for the desired sulfuric acid concentrations. The interpolated index was then corrected for the temperature-dependent sulfuric acid density changes[37] using the Lorentz−Lorenz transform. The resulting real indices at the anchor point for all of the temperatures and compositions studied here are given in Table 2.

The subtractive Kramers−Kronig transform used to calculate the real refractive indices in this work is subject to truncation errors. These errors often manifest themselves as a rapid divergence in the real index at low frequencies. Since our FT-IR spectral data are limited to the 825 cm^{-1} cutoff of our BaF_2 transmission optics, we avoided this truncation problem by artificially extending the data sets to a lower wavenumber. This approach was found to be effective in our previous study of nitric acid dihydrate optical constants.[33] Since there are sulfuric acid absorption bands at low wavenumber, we decided to use the imaginary indices of Palmer and Williams between 400 and 825 cm^{-1} as an estimate of the true form of the imaginary indices, as opposed to a simple exponential decay, beyond our observation region. We performed a spline fit of the Palmer and Williams data set that was closest to the composition at hand, scaled it appropriately, and included in the Kramers−Kronig calculation along with our observed imaginary index data. We found that this extension procedure indeed significantly reduced the amount of divergence in the real index above 825 cm^{-1}.

Results and Discussion

We report here a total of 31 sets of optical constants for liquid sulfuric acid/water between 200 and 300 K and 32−87 wt %. Figure 6 summarizes the data, each point representing a complete frequency-dependent set of complex refractive indices. The regions of the Gable et al.[38] phase diagram that are devoid of points were inaccessible for various reasons. In the lower right-hand corner the vapor pressure of water was too low to be detected using our current TDL arrangement, although further

TABLE 2: "Anchor Point" Real Refractive Index Values Employed in Subtractive Kramers−Kronig Calculations[a]

T (K)	wt % H_2SO_4	*n* at 3800 cm^{-1}
300	85	1.341
300	75	1.320
300	72	1.320
280	85	1.347
280	76	1.324
280	70	1.315
280	63	1.305
280	50	1.286
260	87	1.382
260	76	1.327
260	72	1.321
260	55	1.297
260	47	1.286
260	42	1.268
240	80	1.342
240	69	1.319
240	59	1.306
240	50	1.293
240	42	1.281
230	75	1.331
220	72	1.327
220	66	1.318
220	55	1.303
220	50	1.296
220	43	1.286
220	38	1.277
210	61	1.313
210	39	1.281
210	32	1.270
200	50	1.299
200	45	1.292

[a] These values were determined by the interpolation/extrapolation method described in the text.

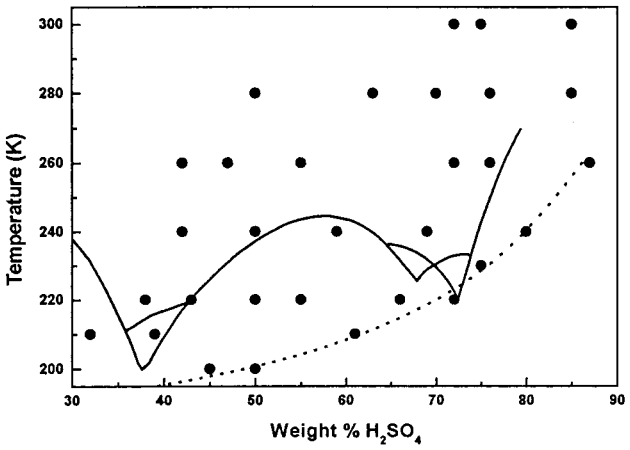

Figure 6. A summary of the 31 optical constant data sets obtained in this study, plotted in the phase diagram of Gable et al.[38] The dotted curve, taken from Steele and Hamill,[39] represents aerosol compositions typical of the stratosphere, given a water vapor partial pressure of 5×10^{-4} mbar.

multipassing of the laser could be used to overcome this difficulty. In the upper left-hand corner of Figure 6, the FT-IR spectra are heavily congested with water vapor absorption lines. We note here that in cases where water vapor transitions appear in the raw FT-IR spectra, they were subtracted out before the data were used to extract optical constants. Nevertheless, when these vapor features become very intense, the subtraction is not perfect, and the resulting data sets show some spurious features. Fortunately, the regions of the phase diagram that are most relevant to the atmosphere (note the stratospheric line of Steele and Hamill[39] in Figure 6) were all accessible using the present technique. The optical constants for several of these relevant points are listed in Table 3.

We tested the present method against the previously published work on sulfuric acid by studying a number of sulfuric acid compositions at room temperature, chosen to match the refractive indices of Palmer and Williams.[6] These results have been presented in our preliminary report[16] but warrant a brief review here. Figure 7 shows a comparison between the PW results for 75 wt %, room temperature sulfuric acid and those obtained from the present experiments. The agreement between the data sets is fairly good, although there are some differences (up to 20%) at longer wavelengths, especially between 800 and 1600 cm^{-1}. This region is dominated by absorption bands associated with sulfate species in the solution, including sulfate ions, bisulfate ions, and molecular sulfuric acid.[5] It is important to note that the PW data sets were determined by measuring near normal reflectance from bulk sulfuric acid solutions and that the imaginary refractive indices were then obtained using a Kramers−Kronig transform. Palmer and Williams report an average error of ±3%, with the error increasing systematically at longer wavelengths, precisely where the discrepancies with the present data set are the greatest.

Further evidence that the differences in this frequency region are associated with errors in the PW data set comes from comparing the results with those of Remsberg et al.,[7] which cover the sulfate region. The latter data set was obtained using attenuated total reflection (ATR), a method which is more precise at longer wavelengths than the technique employed by Palmer and Williams.[30] As shown in Figure 8, the data of Remsberg et al.[7] are in better agreement with the present results. From this, we conclude that the present data sets at room temperature are somewhat better than those of Palmer and Williams over the entire frequency range. Indeed, the differences between the PW and the present data sets are significant when fitting the aerosol spectra reported here. As a further check of our data, optical constants were retrieved from spectra corresponding to a range of particle sizes. In all cases, the real and imaginary indices were in agreement with one another to within ±3%. It is important to point out that in regions where the infrared transmission of the aerosol is high (i.e., at large wavenumber), we estimate that the uncertainty in the imaginary index, determined primarily by spectrometer noise, is ±0.005 index units.

Given the temperature control we have over the cell, it is now straightforward to extend these measurements to lower temperatures. Figure 9 shows a comparison of the data for 75 wt % sulfuric acid at temperatures of 300, 280, and 260 K. At these high concentrations we find that the results are rather insensitive to temperature, with the exception of minor differences in some of the band intensities in the imaginary index data in Figure 9b. In these cases, the vibrational modes of the bisulfate ion (HSO_4^-) and water[5] dominate the infrared extinction spectrum. Since the concentrations of these species are relatively insensitive to temperature for 75 wt %,[28] the optical constants are correspondingly insensitive. This explains why comparisons made by Tisdale et al.[17] in a recent publication of thin film sulfuric acid optical constants at approximately 215 K with the earlier room-temperature results were quite reasonable.

The situation is quite different for more dilute solutions. For example, consider the case of 50 wt % sulfuric acid shown in Figure 10 for 280, 240, 220, and 200 K. The intensities and band shapes in the imaginary index data shown in Figure 10b change significantly with temperature. In particular, the ν_3 band

TABLE 3: Selected Optical Constant Values for Sulfuric Acid at Different Temperatures and Compositions Relevant to the Stratosphere

	240 K, 80 wt %		220 K, 72 wt %		210 K, 61 wt %		200 K, 50 wt %	
cm^{-1}	*k*	*n*	*k*	*n*	*k*	*n*	*k*	*n*
4700.82	0.004	1.389	0.002	1.380	0.002	1.388	0.001	1.375
4600.52	0.004	1.388	0.001	1.376	0.002	1.383	0.001	1.371
4500.21	0.003	1.385	0.001	1.372	0.002	1.378	0.000	1.366
4399.91	0.002	1.380	0.000	1.368	0.002	1.373	0.001	1.361
4299.60	0.005	1.378	0.002	1.363	0.001	1.367	0.001	1.356
4199.30	0.004	1.373	0.002	1.359	0.001	1.360	0.001	1.349
4100.92	0.005	1.367	0.002	1.354	0.002	1.350	0.001	1.342
4000.62	0.004	1.361	0.002	1.347	0.003	1.342	0.001	1.332
3900.31	0.006	1.354	0.002	1.339	0.004	1.330	0.001	1.318
3800.01	0.005	1.342	0.002	1.327	0.004	1.313	0.001	1.299
3699.70	0.006	1.325	0.001	1.309	0.005	1.285	0.002	1.267
3599.40	0.018	1.301	0.016	1.270	0.035	1.230	0.034	1.202
3560.82	0.027	1.294	0.034	1.260	0.062	1.218	0.069	1.183
3520.31	0.037	1.288	0.055	1.255	0.093	1.214	0.112	1.176
3479.80	0.046	1.283	0.074	1.256	0.123	1.217	0.156	1.184
3439.30	0.056	1.279	0.091	1.263	0.152	1.230	0.195	1.206
3400.72	0.066	1.276	0.104	1.270	0.174	1.248	0.225	1.234
3360.21	0.076	1.274	0.114	1.280	0.188	1.271	0.243	1.272
3319.70	0.087	1.271	0.118	1.289	0.193	1.291	0.248	1.305
3279.19	0.099	1.269	0.124	1.294	0.196	1.308	0.248	1.335
3240.62	0.111	1.267	0.129	1.298	0.196	1.322	0.246	1.361
3200.11	0.126	1.267	0.135	1.304	0.195	1.334	0.234	1.387
3159.60	0.142	1.270	0.140	1.309	0.192	1.344	0.220	1.408
3119.09	0.158	1.275	0.145	1.313	0.190	1.350	0.202	1.420
3080.51	0.172	1.282	0.150	1.318	0.189	1.355	0.187	1.426
3040.01	0.187	1.292	0.156	1.324	0.189	1.361	0.173	1.429
2999.50	0.200	1.305	0.164	1.333	0.186	1.366	0.161	1.430
2960.92	0.209	1.318	0.166	1.341	0.187	1.365	0.150	1.426
2920.41	0.218	1.334	0.171	1.345	0.195	1.369	0.149	1.423
2879.90	0.223	1.351	0.172	1.358	0.199	1.378	0.144	1.423
2839.40	0.225	1.369	0.175	1.368	0.201	1.389	0.144	1.423
2800.82	0.222	1.384	0.171	1.380	0.198	1.401	0.139	1.424
2760.31	0.216	1.396	0.167	1.388	0.192	1.409	0.135	1.424
2719.80	0.211	1.406	0.160	1.394	0.185	1.413	0.131	1.425
2679.29	0.205	1.413	0.155	1.396	0.179	1.415	0.127	1.423
2640.72	0.201	1.418	0.153	1.396	0.175	1.415	0.123	1.422
2600.21	0.199	1.423	0.150	1.397	0.172	1.416	0.120	1.419
2559.70	0.197	1.430	0.148	1.399	0.168	1.417	0.116	1.415
2519.19	0.193	1.437	0.146	1.402	0.165	1.416	0.114	1.410
2480.61	0.189	1.443	0.144	1.403	0.163	1.415	0.114	1.405
2440.11	0.182	1.450	0.139	1.405	0.160	1.413	0.115	1.400
2399.60	0.172	1.454	0.133	1.404	0.159	1.409	0.119	1.395
2359.09	0.161	1.451	0.132	1.400	0.160	1.404	0.125	1.392
2320.51	0.157	1.443	0.132	1.397	0.163	1.402	0.128	1.391
2280.00	0.161	1.436	0.134	1.391	0.166	1.400	0.132	1.390
2239.50	0.170	1.437	0.137	1.392	0.168	1.402	0.134	1.391
2220.21	0.173	1.442	0.138	1.394	0.168	1.402	0.135	1.391
2200.92	0.174	1.448	0.138	1.396	0.168	1.402	0.135	1.391
2179.70	0.172	1.455	0.136	1.397	0.166	1.403	0.135	1.389
2139.19	0.161	1.464	0.130	1.395	0.162	1.399	0.135	1.387
2100.61	0.148	1.464	0.126	1.392	0.160	1.392	0.136	1.383
2060.11	0.137	1.458	0.122	1.382	0.160	1.381	0.137	1.376
2019.60	0.129	1.448	0.123	1.371	0.164	1.368	0.141	1.368
1979.09	0.126	1.436	0.126	1.356	0.172	1.353	0.149	1.357
1940.51	0.128	1.423	0.137	1.344	0.187	1.338	0.160	1.346
1900.00	0.134	1.411	0.152	1.329	0.211	1.325	0.181	1.337
1869.14	0.142	1.403	0.169	1.321	0.234	1.320	0.200	1.335
1840.21	0.152	1.398	0.189	1.318	0.261	1.321	0.221	1.338
1809.34	0.164	1.396	0.214	1.319	0.290	1.330	0.243	1.347
1780.41	0.177	1.397	0.240	1.330	0.319	1.349	0.265	1.364
1749.55	0.191	1.404	0.262	1.352	0.342	1.382	0.280	1.392
1720.61	0.202	1.420	0.278	1.385	0.353	1.425	0.283	1.423
1710.97	0.203	1.426	0.279	1.399	0.351	1.443	0.280	1.434
1699.39	0.203	1.434	0.277	1.417	0.344	1.462	0.274	1.444
1670.46	0.196	1.457	0.251	1.452	0.310	1.499	0.259	1.462
1639.60	0.166	1.474	0.210	1.468	0.262	1.512	0.238	1.483
1610.66	0.133	1.466	0.173	1.459	0.219	1.502	0.203	1.487
1579.80	0.109	1.443	0.144	1.433	0.189	1.467	0.177	1.466
1550.87	0.097	1.416	0.137	1.402	0.181	1.435	0.169	1.445
1520.00	0.090	1.385	0.137	1.372	0.184	1.403	0.169	1.425

TABLE 3: (Continued)

	240 K, 80 wt %		220 K, 72 wt %		210 K, 61 wt %		200 K, 50 wt %	
cm^{-1}	*k*	*n*	*k*	*n*	*k*	*n*	*k*	*n*
1489.14	0.091	1.352	0.142	1.348	0.193	1.377	0.173	1.409
1460.21	0.093	1.319	0.150	1.322	0.203	1.355	0.180	1.396
1429.34	0.099	1.275	0.166	1.297	0.215	1.331	0.187	1.383
1400.41	0.119	1.221	0.176	1.269	0.232	1.301	0.193	1.366
1369.55	0.157	1.162	0.203	1.225	0.260	1.276	0.211	1.352
1340.61	0.222	1.095	0.251	1.195	0.290	1.252	0.218	1.346
1309.75	0.345	1.069	0.309	1.183	0.325	1.236	0.229	1.325
1280.81	0.426	1.090	0.342	1.170	0.345	1.196	0.246	1.296
1249.95	0.521	1.070	0.421	1.108	0.432	1.111	0.283	1.255
1219.09	0.690	1.113	0.592	1.121	0.604	1.108	0.359	1.227
1211.37	0.728	1.141	0.629	1.146	0.641	1.123	0.377	1.226
1199.80	0.779	1.191	0.676	1.187	0.693	1.150	0.406	1.222
1188.23	0.818	1.249	0.710	1.231	0.745	1.178	0.441	1.220
1176.65	0.848	1.309	0.749	1.274	0.804	1.219	0.482	1.224
1172.79	0.856	1.328	0.765	1.293	0.822	1.240	0.498	1.226
1168.94	0.864	1.347	0.775	1.313	0.836	1.261	0.512	1.230
1163.15	0.878	1.378	0.794	1.347	0.858	1.295	0.534	1.238
1159.29	0.886	1.398	0.798	1.372	0.867	1.323	0.547	1.243
1155.43	0.897	1.421	0.808	1.397	0.870	1.350	0.564	1.250
1151.58	0.906	1.448	0.807	1.427	0.869	1.373	0.578	1.257
1147.72	0.914	1.478	0.808	1.451	0.868	1.392	0.595	1.267
1143.86	0.919	1.514	0.805	1.481	0.867	1.412	0.609	1.279
1140.00	0.913	1.550	0.795	1.510	0.862	1.431	0.622	1.291
1136.14	0.904	1.583	0.778	1.533	0.855	1.444	0.632	1.303
1132.29	0.891	1.615	0.760	1.550	0.852	1.455	0.647	1.315
1120.71	0.826	1.686	0.717	1.589	0.849	1.476	0.680	1.358
1109.14	0.754	1.717	0.672	1.599	0.859	1.502	0.709	1.410
1097.57	0.687	1.705	0.655	1.589	0.875	1.539	0.727	1.470
1089.85	0.664	1.675	0.643	1.591	0.864	1.565	0.732	1.510
1085.99	0.661	1.656	0.639	1.580	0.866	1.566	0.730	1.533
1082.13	0.667	1.635	0.639	1.572	0.869	1.569	0.727	1.550
1078.28	0.682	1.615	0.646	1.556	0.876	1.569	0.726	1.566
1070.56	0.742	1.597	0.687	1.542	0.913	1.571	0.728	1.605
1058.99	0.849	1.655	0.763	1.571	0.988	1.635	0.707	1.661
1055.13	0.874	1.695	0.779	1.597	1.011	1.670	0.700	1.676
1051.27	0.891	1.740	0.800	1.625	1.026	1.712	0.695	1.692
1043.56	0.897	1.841	0.826	1.702	1.035	1.805	0.686	1.732
1035.84	0.869	1.940	0.814	1.785	1.022	1.904	0.660	1.773
1028.12	0.807	2.030	0.778	1.860	0.971	2.003	0.624	1.808
1024.27	0.765	2.065	0.748	1.893	0.930	2.041	0.605	1.822
1020.41	0.718	2.093	0.719	1.918	0.890	2.069	0.584	1.834
1008.83	0.569	2.118	0.616	1.956	0.760	2.127	0.514	1.853
1004.98	0.525	2.110	0.588	1.960	0.713	2.131	0.491	1.853
1001.12	0.485	2.097	0.554	1.959	0.669	2.127	0.468	1.848
989.55	0.398	2.036	0.487	1.933	0.579	2.076	0.430	1.803
977.97	0.362	1.980	0.453	1.915	0.550	2.069	0.425	1.815
970.26	0.342	1.948	0.418	1.903	0.504	2.057	0.410	1.823
966.40	0.336	1.933	0.402	1.892	0.487	2.048	0.386	1.822
958.68	0.319	1.904	0.381	1.873	0.452	2.026	0.365	1.814
950.97	0.307	1.866	0.368	1.850	0.425	1.992	0.347	1.802
943.25	0.307	1.817	0.359	1.823	0.410	1.962	0.332	1.788
935.53	0.335	1.762	0.359	1.793	0.409	1.927	0.323	1.774
927.82	0.400	1.723	0.378	1.760	0.421	1.898	0.319	1.759
923.96	0.444	1.719	0.389	1.745	0.430	1.888	0.320	1.753
916.25	0.532	1.755	0.442	1.741	0.463	1.879	0.319	1.745
912.39	0.568	1.792	0.467	1.748	0.481	1.885	0.319	1.742
904.67	0.605	1.898	0.514	1.789	0.508	1.913	0.320	1.739
900.81	0.599	1.956	0.528	1.828	0.513	1.939	0.321	1.740
896.96	0.578	2.011	0.522	1.863	0.508	1.963	0.319	1.740
893.10	0.543	2.060	0.517	1.895	0.498	1.984	0.318	1.741
885.38	0.444	2.114	0.477	1.957	0.460	2.021	0.309	1.742
881.52	0.396	2.120	0.447	1.977	0.437	2.031	0.308	1.741
873.81	0.316	2.102	0.381	1.996	0.382	2.030	0.302	1.737
869.95	0.291	2.090	0.354	1.992	0.368	2.020	0.300	1.736
862.24	0.245	2.068	0.305	1.984	0.340	2.015	0.295	1.742
858.38	0.224	2.056	0.283	1.975	0.321	2.009	0.286	1.742
850.66	0.189	2.028	0.247	1.950	0.291	1.983	0.270	1.731
846.80	0.174	2.012	0.235	1.936	0.283	1.967	0.266	1.724
839.09	0.151	1.978	0.218	1.911	0.276	1.943	0.265	1.711
827.51	0.138	1.935	0.200	1.882	0.268	1.921	0.263	1.701

of the sulfate ion (SO_4^{2-}) at 1105 cm^{-1} becomes significantly more intense as the temperature decreases, with a corresponding decrease in intensity of bands attributed to the bisulfate ion.[5] There is also an obvious red shift of the O−H stretching band

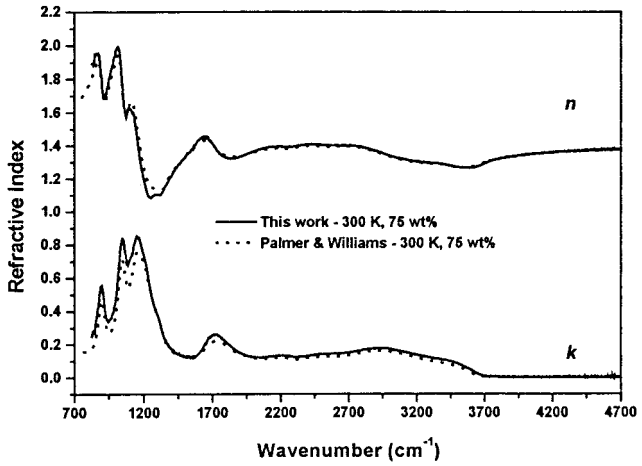

Figure 7. Comparison of room temperature, 75 wt % optical constants derived from aerosol spectra in this work (solid) and from bulk solutions by Palmer and Williams[6] (dotted). In general, the data agree well, although there are intensity differences at lower frequencies, possibly related to errors in the Palmer and Williams data (see text).

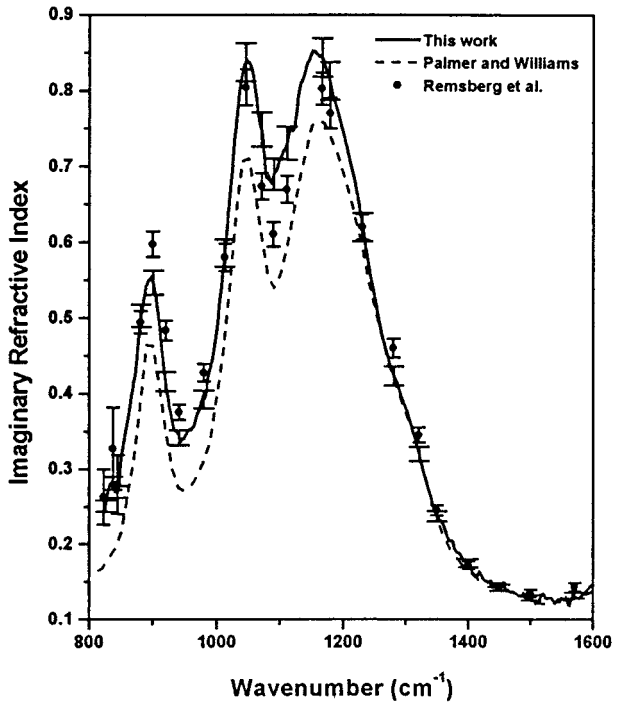

Figure 8. Comparison of room temperature, 75 wt % optical constants derived from aerosol spectra in this work (solid) and from bulk solutions by Palmer and Williams[6] (dotted) and Remsberg et al.[7] (circles). The Remsberg et al. data, which tends to agree better with the current results, within the error bars reported for each data set, were determined over this limited range using a spectroscopic technique that is generally more accurate than that of Palmer and Williams (see text).

at 3 μm. All of these data are consistent with the Carslaw et al.[28] model for the concentration of the ions, which shows that the equilibrium shifts toward the sulfate ion as the temperature is lowered. The red shift in the O−H band can then be explained as being a result of the stronger hydrogen bonding between the water and the sulfate ion, compared to those associated with the bisulfate species. Even more dramatic changes are seen at 38 wt %,[16] where there are approximately eight water molecules per ion, optimizing the hydrogen bonding network and making these effects the most prominent. Tisdale et al.[17] also noted that the differences between the room temperature and the colder optical constants were larger for more dilute solutions. However,

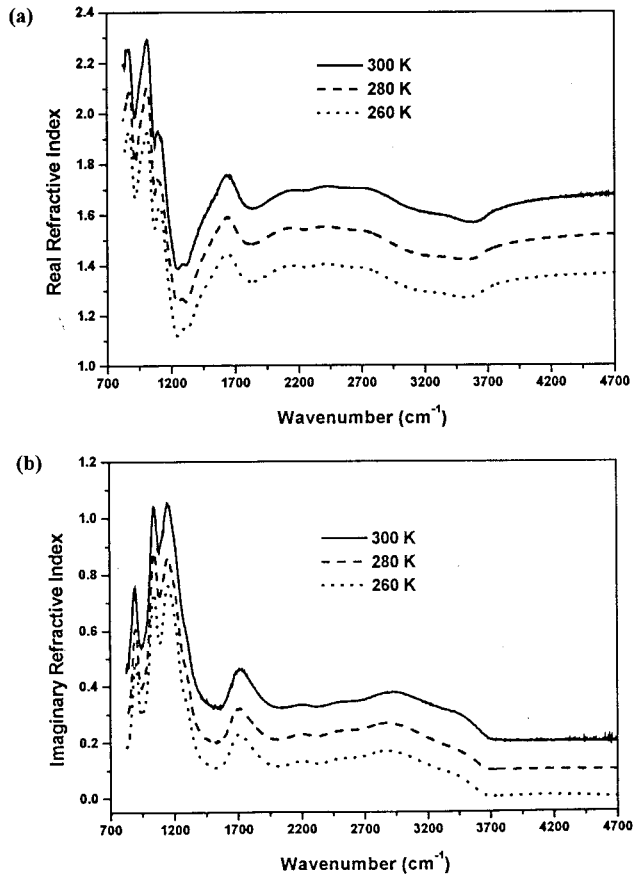

Figure 9. Temperature dependence of real (a) and imaginary (b) refractive indices for 75 wt % aerosols. The 260 K data sets are true values, while the others are offset for clarity.

since their studies were only performed at one temperature, they were unable to differentiate between temperature and composition effects, and they did not correlate these differences with the ionic equilibrium shift.[17]

We can now make direct comparisons between the results reported here and those published by Tisdale et al.,[17] which were retrieved from sulfuric acid thin films with compositions between 45 and 80 wt % at approximately 215 K. For the more concentrated solutions (72 and 66 wt % from the present study compared to the Tisdale et al.[17] 70.2 and 65.3 wt % data), the agreement is within the experimental error. However, the agreement is not as good for the more dilute solutions (55, 50, and 45 wt %), as shown in Figure 11. Although the agreement is excellent above 1300 cm^{-1}, there are significant differences at longer wavelengths, where strong absorption bands associated with HSO_4^- and SO_4^{2-} dominate the imaginary refractive indices. Such discrepancies could have a significant impact on how accurately aerosol characteristics are determined from spectroscopic remote sensing data.

In considering the source of these differences, we begin with the possibility that the aerosol and/or thin film experiments may have errors in their composition determinations. In the Tisdale et al.[17] study, the film compositions were determined using a method based on integrating the areas under bands near 3300 cm^{-1} corresponding to molecular H_2SO_4 and water in the thin film spectra of calibrated samples. To further test the reliability of this method, we have used it to analyze our own nonscattering aerosol spectra recorded at 220 K. In Figure 12, we show a number of the resulting area ratios plotted as a function of the composition determined by measuring water vapor pressures with the TDL, compared to the Tisdale et al.[17] calibration curve.

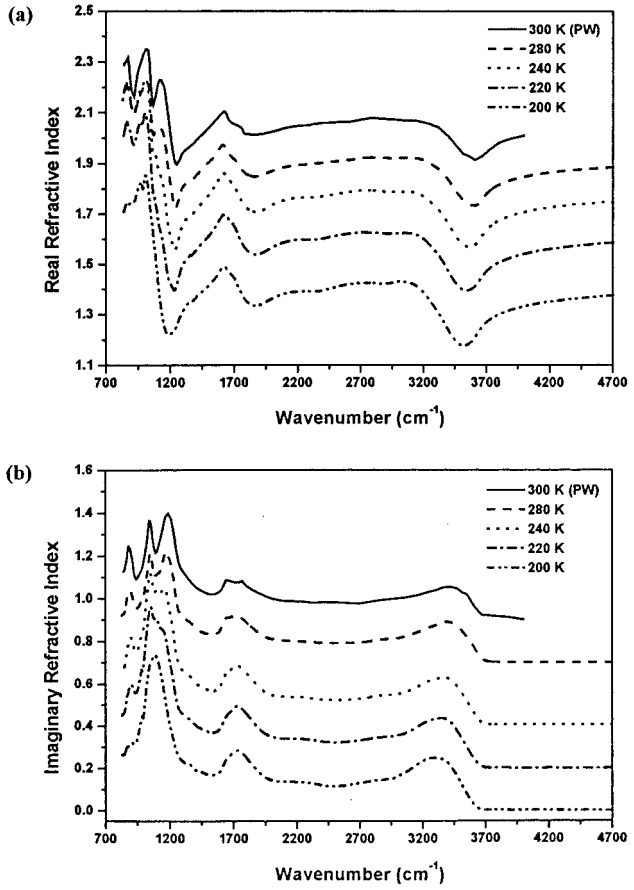

Figure 10. Temperature dependence of real (a) and imaginary (b) refractive indices for 50 wt % aerosols from 200 to 280 K and at 300 K by Palmer and Williams.[6] The 200 K data sets are true values, while the others are offset for clarity.

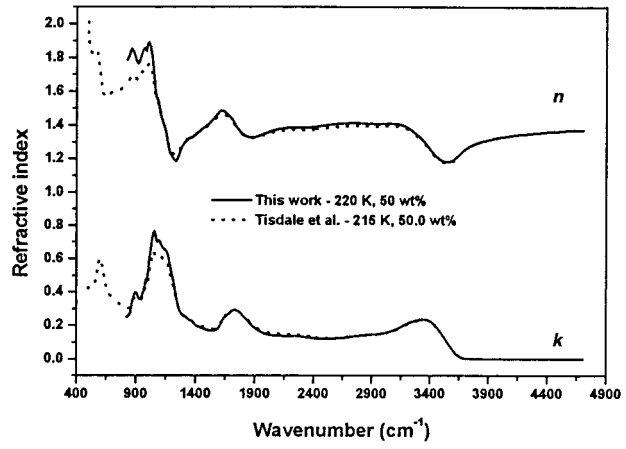

Figure 11. Comparison of 50 wt % optical constants derived from aerosol spectra at 220 K in this work (solid) and from thin films at approximately 215 K by Tisdale et al.[17] Aside from intensity differences in the sulfate region from 900 to 1300 cm^{-1}, the data agree rather well across the frequency range.

The agreement is clearly excellent at this temperature, suggesting that the two methods for determining composition are consistent with one another. We have also tested the temperature dependence of this area method using nonscattering aerosol spectra collected from 200 to 280 K, and found that it is reliable over this range. It is therefore apparent that composition determination is not a problem.

It is interesting to note that the Tisdale et al.[17] data is an average over a number of data sets recorded over a temperature range up to 19 K near 215 K. Therefore, another possibility for the differences is that an error is introduced into their results as a result of the ion equilibrium shift with temperature discussed above. In Figure 13, we compare the 50.0 wt %, ~215 K imaginary indices of Tisdale et al.,[17] to the present 50 wt % indices for a range of temperatures. Once again, there is excellent agreement (within experimental error) above 1300 cm^{-1} among the data sets. As shown in the insert, however, the ~215 K thin film data agrees better with the present indices at higher temperatures. Thus, the variation in the film temperatures in the Tisdale et al.[17] study might partially account for the differences based on a corresponding change in the equilibrium of bisulfate and sulfate ions. This is consistent with the

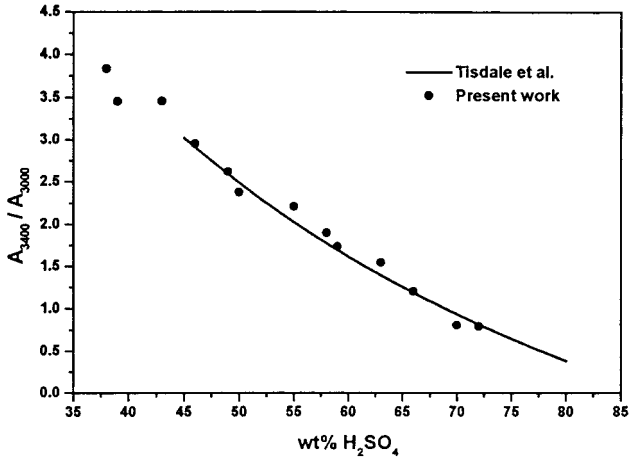

Figure 12. Area ratios (circles) calculated using the spectral integration method of Tisdale et al.[17] for nonscattering aerosols in this work, plotted against the compositions determined from diode laser vapor pressure measurements. These data are in excellent agreement with the Tisdale et al. curve (solid line) determined from calibrated thin film transmission spectra.

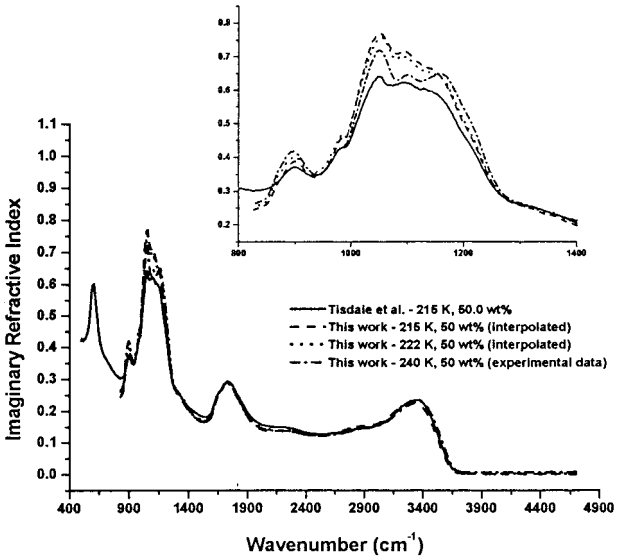

Figure 13. Comparison of 50 wt % imaginary refractive indices at approximately 215 K by Tisdale et al.[17] (solid) to those at various temperatures from this work. The interpolated data sets were retrieved using the method described in the text. All of the data sets shown agree well at high frequencies, but in the lower frequency sulfate region (inset), the Tisdale et al. $k(\nu)$ values are much lower than ours at 215 K. At 222 K, the highest temperature reported for the 50 wt % films by Tisdale et al.,[17] the agreement is slightly better. The ~215 K thin film imaginary indices most closely match the present results at 240 K.

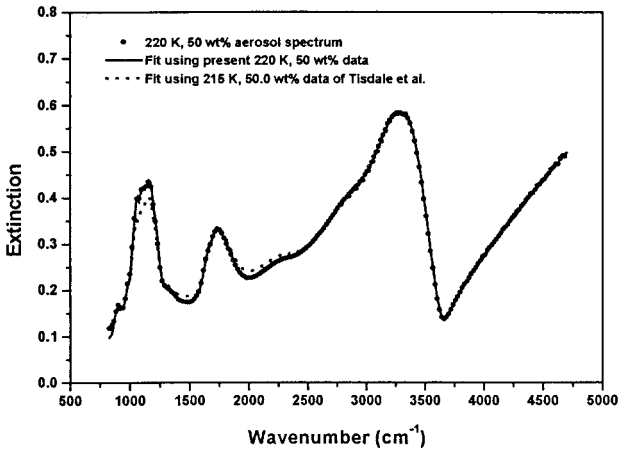

Figure 14. Mie simulations to an experimental aerosol spectrum (some points skipped for clarity) recorded in this work. Both the present refractive indices and those of Tisdale et al.[17] converged to log-normal size distribution parameters of $r_{med} = 0.35$ μm and $\sigma = 0.45$, though the present results better simulate the entire extinction profile.

observation that in the three 50 wt % thin film absorbance spectra published by Tisdale et al.,[17] the relative band intensities associated with HSO_4^- and SO_4^{-2} near 1100 cm^{-1} are somewhat different. The authors point out in their paper that this "spectral mismatching" results in larger errors in this region of the spectrum. Nevertheless, even with this taken into account, we are left with a difference between the two data sets that is somewhat larger than the sum of the estimated errors for both. We have used the present results and the Tisdale et al.[17] data in Mie scattering simulations of the particle extinction spectra collected in our flow cell apparatus. Since the two data sets are essentially the same above 1300 cm^{-1}, where the scattering contribution is significant and the spectra are very sensitive to particle size, they result in very similar size distributions. Nevertheless, as shown in Figure 14, the thin film data[17] fails to faithfully reproduce the extinction profile near 1100 cm^{-1}.

Although we have focused here on the differences between these two data sets, what is perhaps more impressive is the agreement. Given that the methods used in the two studies are very different, the combination of the two serve to provide a very good idea concerning the reliability of these optical constants. The present study clearly illustrates the importance of using optical constants that correspond to not only the correct composition but also the temperature appropriate to the atmosphere. To facilitate use of the present database in remote sensing applications, we have developed a FORTRAN program to interpolate in two dimensions among our data sets, so that optical constants can be generated at any concentration and temperature required, as shown in Figure 13. We have tested this interpolation scheme within the portion of the phase diagram sampled by removing a data set from the database and generating an interpolated data set for comparison. We have further tested the routine by collecting FT-IR aerosol extinction spectra at several temperatures and compositions other than the 31 points reported here, and simulating those spectra using interpolated refractive indices in Mie theory calculations. In these cases, the residual difference between the experimental and calculated spectra was less than 0.1%. This interpolation program (executable code only), as well as all of the optical constant data sets (ASCII format) indicated in Figure 6, is available from the authors directly or by anonymous FTP to ftp://frenchie.chem.unc.edu.

Summary

In the present study we have obtained the most extensive database of optical constants for the binary sulfuric acid/water system yet reported, spanning essentially the entire range of atmospherically relevant temperatures and compositions. The current study also provides spectroscopic results that should contribute to our understanding of the nature of the intermolecular interactions in these ionic solutions. By varying the solution temperatures, we have shifted the ionic equilibria and examined the effects this has on the ion−water solvent network through observing changes in the O−H vibrational band. Of particular interest is the 38 wt % solution,[16] which has approximately eight water molecules per ion, such that essentially every water molecule is in a first solvation shell. Not too surprisingly, the 3300 cm^{-1} O−H vibrational band is observed to shift strongly to the red and to intensify as the ionic equilibrium shifts from the singly charged bisulfate ion (HSO_4^-) to the doubly charged sulfate ion (SO_4^{-2}). We would expect this change to result in a strengthening of the ion−water solvent hydrogen bonding, resulting in the red shift and increased band intensity. Comparisons of these observations with theoretical calculations might therefore provide interesting new insights into the nature of the interactions within these solutions.

Acknowledgment. Financial support for this work is gratefully acknowledged from the NASA Upper Atmospheres Research Program (UARP) Grant NAG5-3946.

References and Notes

(1) Toon, O. B.; Turco, R. P. *Sci. Am.* **1991**, *264*, 68.
(2) Lacis, A. A.; Mishchenko, M. I. Climate Forcing, Climate Sensitivity, and Climate Response: A Radiative Modeling Perspective on Atmospheric Aerosols. In *Aerosol Forcing of Climate;* Charlson, R. J., Heintzenberg, J., Eds.; John Wiley & Sons: New York, 1995.
(3) Rinsland, C. P.; Yue, G. K.; Gunson, M. R.; Zander, R.; Abrams, M. C. *J. Quantum Spec. Rad. Trans.* **1994**, *52*, 241.
(4) Grainger, R. G.; Lambert, A.; Rogers, C. D.; Taylor, F. W.; Deshler, T. *J. Geophys. Res.* **1995**, *100*, 16507.
(5) Querry, M. R.; Waring, R. C.; Holland, W. E.; Earls, L. M.; Herrman, M. D.; Nijm, W. P.; Hale, G. M. *J. Opt. Soc. Am.* **1974**, *64*, 39.
(6) Palmer, K. F.; Williams, D. *Appl. Opt.* **1975**, *14*, 208.
(7) Remsberg, E. E.; Lavery, D.; Crawford, J. *J. Chem. Eng. Data* **1974**, *19*, 263.
(8) Pinkley, L. W.; Williams, D. *J. Opt. Soc. Am.* **1976**, *66*, 122.
(9) Kiehl, J. T.; Briegleb, B. P. *Science* **1993**, *260*, 311.
(10) Arnold, F. *Ber. Bunsen-Ges. Phys. Chem.* **1992**, *96*, 339.
(11) Wooldridge, P. J.; Zhang, R.; Molina, M. J. *J. Geophys. Res.* **1995**, *100*, 1389.
(12) Clapp, M. L.; Niedziela, R. F.; Richwine, L. J.; Dransfield, T.; Miller, R. E.; Worsnop, D. R. *J. Geophys. Res.* **1997**, *102*, 8899.
(13) Dawson, B. S. W.; Irish, D. E.; Toogood, G. E. *J. Phys. Chem.* **1986**, *90*, 334.
(14) Bertram, A. K.; Patterson, D. D.; Sloan, J. J. *J. Phys. Chem.* **1996**, *100*, 2376.
(15) Martin, S. T.; Salcedo, D.; Molina, L. T.; Molina, M. J. *J. Phys. Chem.* **1997**, *101*, 5307.
(16) Niedziela, R. F.; Norman, M. L.; Miller, R. E.; Worsnop, D. R. *Geophys. Res. Lett.* **1998**, *25*, 4477.
(17) Tisdale, R. T.; Glandorf, D. L.; Tolbert, M. A.; Toon, O. B. *J. Geophys. Res.* **1998**, *103*, 25353.
(18) Ritzhaupt, G.; Devlin, J. P. *J. Phys. Chem.* **1991**, *95*, 90.
(19) Toon, O. B.; Tolbert, M. A.; Koehler, B. G.; Middlebrook, A. M.; Jordan, J. *J. Geophys. Res.* **1994**, *99*, 25631.
(20) Iraci, L. T.; Fortin, T. J.; Tolbert, M. A. *J. Geophys. Res.* **1998**, *103*, 8491.
(21) Tolbert, M. A.; Koehler, B. G.; Middlebrook, A. M. *Spectrochim. Acta* **1992**, *48*, 1363.
(22) Koehler, B. G.; Middlebrook, A. M.; Tolbert, M. A. *J. Geophys. Res.* **1992**, *97*, 8065.
(23) Clapp, M. L.; Worsnop, D. R.; Miller, R. E. *J. Phys. Chem.* **1995**, *99*, 6317.
(24) Lovejoy, E. R.; Huey, L. G.; Hanson, D. R. *J. Geophys. Res.* **1995**, *100*, 18, 775.
(25) Houghton, G. *J. Chem. Phys.* **1964**, *40*, 1628.

(26) Luo, B. P.; Clegg, S. L.; Peter, Th.; Muller, R.; Crutzen, P. J. *Geophys. Res. Lett.* **1994**, *21*, 49.

(27) Anthony, S. E.; Tisdale, R. T.; Disselkamp, R. S.; Tolbert, M. A. *Geophys. Res. Lett.* **1995**, *22*, 1105.

(28) Carslaw, K. S.; Clegg, S. L.; Brimblecombe, P. *J. Phys. Chem.* **1995**, *99*, 11557.

(29) Rothman, L. S.; Gamache, R. R.; Tipping, R. H.; Rinsland, C. P.; Smith, M. A. H.; Benner, D. C.; Devi, V. M.; Flaud, J.-M.; Camy-Peyret, C.; Perrin, A.; Goldman, A.; Massie, S. T.; Brown, L. R.; Toth, R. A. *J. Quant. Spectrosc. Radiat. Trans.* **1992**, *48*, 469.

(30) Ingle, J. D.; Crouch, S. R. *Spectrochemical Analysis;* Prentice Hall: Englewood Cliffs, **1988**.

(31) Goody, R. *Principles of Atmospheric Physics and Chemistry*; Oxford University Press: New York, 1995.

(32) Marti, J.; Mauersberger, K. *Geophys. Res. Lett.* **1993**, *20*, 363.

(33) Niedziela, R. F.; Miller, R. E.; Worsnop, D. R. *J. Phys. Chem.* **1998**, *102*, 6477.

(34) Bohren, C. F.; Huffman, D. R. *Absorption and Scattering of Light by Small Particles*; John Wiley & Sons: New York, 1983.

(35) Palmer, K. F.; Wood, B. E.; Roux, J. A. AEDC-TR-80−30 **1981**, (AD-AO94214).

(36) Hale, G. M.; Querry, M. R. *Appl. Opt.* **1973**, *12*, 555.

(37) Huthwelker, T.; Peter, Th.; Luo, B. P.; Clegg, S. L.; Carslaw, K. S.; Brimblecombe, P. *J. Atmos. Chem.* **1995**, *21*, 81.

(38) Gable, C. M.; Betz, H. F.; Maron, S. H. *J. Am. Chem. Soc.* **1950**, *72*, 1445.

(39) Steele, H. M.; Hamill, P. *J. Aerosol Sci.* **1981**, *12*, 517.